CrossMark

ORIGINAL PAPER

Grain boundary wetness of partially molten dunite

Shangshang Mu[1] · Ulrich H. Faul[2]

Abstract Samples of Fo_{90} olivine and basaltic melt were annealed at a range of temperatures and a pressure of 1 GPa in a piston cylinder apparatus from 1 to 336 h. Post-run samples have melt contents from 0.3 to 6.8 % and mean grain sizes from 4.3 to 84.5 µm. Grain boundary wetness, a measure of the intergranular melt distribution, was determined by analyzing scanning electron microscope images with sufficiently high resolution to detect thin layers wetting grain boundaries, as well as small triple junctions. The measurements show that grain boundary wetness increases with increasing melt content to values well above those predicted by the idealized isotropic equilibrium model for a finite dihedral angle. Additionally, the melt geometry changes with grain size, with grain boundary wetness increasing with increasing grain size at fixed melt content. Grain boundary wetness and dihedral angle of samples annealed at a range of temperatures, but constant melt content does not depend on temperature. These observations emphasize that the dihedral angle alone is not adequate to characterize the melt distribution in partially molten rocks, as the idealized isotropic model does not account for the influence of grain growth. Diffusion creep viscosities calculated from the measured wetness reflect the grain size

and melt content dependence. Accordingly, experimentally measured viscosities at small grain sizes underestimate the effect of melt to weaken partially molten rocks for coarser grain sizes. The presence of melt in the mantle may therefore enhance diffusion creep relative to dislocation creep.

Introduction

The grain scale distribution of melt plays a key role for physical properties of partially molten regions in Earth's upper mantle (Shankland and Waff 1977; Hirth and Kohlstedt 1995; Faul 2001; ten Grotenhuis et al. 2005; Yoshino et al. 2009). The physical principle governing the grain scale melt distribution in partially molten rocks is the surface energy between crystalline grains and melt (Waff and Bulau 1979; Bulau et al. 1979). This was originally expressed as a balance of surface tensions, establishing a dihedral angle between two grains and melt. For a dihedral angle >0° and up to 60°, grain boundaries are melt free, and the melt forms an interconnected network along three-grain edges (triple junctions) at all melt fractions. For dihedral angles >60°, a threshold melt fraction is needed to form an interconnected network. A dihedral angle of 0° implies complete wetting of all grain boundaries. The model developed for the three-dimensional melt distribution based on surface tension equilibrium assumes grains of a fixed size with space-filling geometry and isotropic surface energy. The predicted melt geometry has constant interfacial curvature and is self-similar, i.e., independent of grain size and melt fraction (von Bargen and Waff 1986).

Correspondingly the dihedral angle for this model is single valued, independent of melt fraction, grain size and the orientations of neighboring grains.

Experimental observations indicate that the melt geometry of partially molten rocks is not adequately described by this idealized isotropic equilibrium model (Waff and Faul 1992; Faul et al. 1994; Faul 1997). Observations from experimental samples show that melt forms not only triple junctions with constant interfacial curvature, but also larger pockets surrounded by four or more grains with faceted crystal–melt interfaces. Faceting of crystal surfaces is prevalent and due to anisotropic surface energy of olivine, first noted by Cooper and Kohlstedt (1982). High-resolution imaging shows that triple junctions include smoothly curved, as well as faceted interfaces (Cmíral et al. 1998). Faceted crystal–melt interfaces are slow growing and tend to stabilize the melt pockets (Waff and Faul 1992). Importantly melt also wets some, but not all, grain boundaries (Faul 1997; Garapić et al. 2013).

Experimental observations therefore imply that the melt geometry in partially molten systems cannot be characterized by a single dihedral angle alone. A parameter is needed that better accounts for the variability of the melt geometry observed in partially molten rocks. Dividing the melt geometry into different geometrical categories (Faul 1997; Cmíral et al. 1998) incurs the problem that the division is necessarily somewhat arbitrary, as a continuous range of geometries is observed. A relatively straightforward parameter that is model independent and includes measurement of the total interfacial area (length) is the grain boundary wetness ψ (Takei 1998, 2002). It is defined as the ratio of the length of solid–liquid boundaries (L_{sl}) divided by the total grain boundary length (solid–liquid + solid–solid, Yoshino et al. 2005):

$$\psi = \frac{L_{sl}}{L_{sl} + 2L_{ss}} \tag{1}$$

The factor of 2 in front of L_{ss} arises because each grain boundary involves two crystals. Since grain growth is an important aspect of the melt geometry as discussed below, the wetness needs to be determined for a range of grain sizes. The measurements need to be made over a sufficiently large area to be representative of the melt distribution and at sufficiently high resolution to include melt cusps deeply penetrating between two grains, as well as fully wetted grain boundaries (Garapić et al. 2013).

Methods

Experimental setup

The starting material for the experiments consisted of solution-gelation-derived Fo_{90} olivine powder with a mean

grain size of 1 μm. For details of the preparation of the powder see Jackson et al. (2002) and Faul and Jackson (2007). The olivine powder was mixed with oxide-derived basaltic glass powder by grinding in an agate mortar. The basaltic glass composition was designed to be in equilibrium with a four-phase lherzolite at 1250 °C and 300 MPa (composition: 11.6 % MgO, 13.9 % Al_2O_3, 47.9 % SiO_2, 10.7 % CaO, 2.4 % TiO_2, 10.7 % FeO, 2.2 % Na_2O and 0.5 % K_2O; Cmíral et al. 1998).

All experiments were carried out in a 1.27-cm-diameter end-loaded piston cylinder apparatus at a pressure of 1 GPa and temperatures from 1250 to 1450 °C for 1 to 336 h (Table 1). Only anhydrous components were used for the furnace assembly consisting of an outer NaCl sleeve, Pyrex glass sleeve, graphite heater and MgO inner spacers. The top MgO spacer was drilled out for an alumina thermocouple sleeve. The capsule was separated from the graphite heater by a thin alumina sleeve. This fully dense alumina sleeve also ensured a regular cylindrical shape of the capsule during initial compression. An alumina disk was placed between the thermocouple and the capsule to prevent penetration of the thermocouple into the capsule. The height of capsule plus sample at pressure and temperature was about 2 mm. All furnace components were kept in a drying oven at 105 °C for at least 24 h before use.

Temperature and run duration were controlled with a Eurotherm controller using a type B (Pt–Rh) thermocouple. The power was manually increased until the temperature reached 400 °C. The temperature was then ramped up by the controller at 50 °C/min until it reached the target temperature. At the end of an experiment the samples were quenched by turning off the power to the furnace, followed by pressure release.

The sample material was encapsulated in high-purity graphite capsules, except for one sample that was encapsulated in a FeNi alloy. Three experiments were conducted in graphite–Pt double capsules. As indicated in Table 1, some capsules were heat-treated at 450 °C in a muffle furnace after loading of the sample, while others were not dried prior to assembly. Powders that are not dried to at least 400 °C prior to sealing of a capsule contain adsorbed water (Médard et al. 2008). This water is lost during experiments in anhydrous furnace assemblies such as those used in this study (Truckenbrodt and Johannes 1999; Freda et al. 2001). Double capsules (graphite–Pt) and metal capsules retard the water loss compared to graphite capsules only surrounded by Al_2O_3 or MgO. The (initial) presence of water promotes fast grain growth (Karato 1989), which helps establishing a steady-state grain size and melt distribution. Because of the variable initial water content the grain sizes at the end of the experiments of this study were not consistent with the grain growth kinetics determined from uniformly dried powders (Faul and Scott 2006).

Table 1 Summary of run conditions and image analysis results

Sample	T (°C)	t (h)	Capsule	Conditioning	Wetness (ψ)	Melt fraction	Gr. size (µm)	# of grains
MELT4	1350	120	gr–Pt	–	0.69	0.041	40.5	109
MELT5	1350	27	gr–Pt	–	0.38	0.022	25.3	136
MELT10	1350	81	gr–Pt	–	0.19	0.004	30.9	120
MELT13	1350	336	NiFe	–	0.52	0.019	49.8	137
MELT18	1350	288	gr	Pre-dry[1]	0.14	0.003	15.3	170
MELT19	1350	1	gr	Pre-dry	0.1	0.003	8.9	180
MELT20	1350	1	gr	Pre-dry	0.38	0.030	8.6	340
MELT21	1350	1	gr	Pre-dry	0.23	0.011	8.7	135
MELT22	1350	336	gr	Pre-dry	0.22	0.006	31.2	438
MELT23	1400	336	gr	–	0.76	0.068	84.5	122
MELT24	1350	1	gr	Pre-dry	0.21	0.011	7.8	166
MELT25	1400	130	gr	–	0.43	0.017	43.0	108
MELT27	1250	1	gr	–	0.19	0.010	4.3	327
MELT28	1450	1	gr	Pre-dry	0.34	0.021	13.5	122
MELT29	1250	72	gr	–	0.27	0.019	8.6	269
MELT30	1250	140	gr	–	0.34	0.019	12.9	147
MELT31	1250	361	gr	–	0.21	0.009	12.6	249
MELT33	1350	304	gr	[2]	0.27	0.015	17.5	167

[1] Contains graphite particles on grain boundaries that slowed grain growth

[2] Temperature was unstable, likely due to furnace problems

Temperature distribution in the furnace assembly

An aim of the experiments was to obtain a melt distribution that was homogeneous across the capsule. In the presence of a temperature gradient melt segregates to the hot end in a process similar to zone refining (Lesher and Walker 1988). During temperature-driven segregation channels are established that lead toward melt accumulations at the hot end. The melt distribution and geometry are therefore influenced by factors other than surface energy minimization.

To determine the hot zone of the furnace assembly, axial temperature profiles were mapped by conducting a number of temperature calibration experiments following the method of Watson et al. (2002). This method uses the fact that Al_2O_3 reacts with MgO at high pressures and temperatures to form a spinel layer. The width of the spinel layer is a function of temperature, pressure and time (Watson et al. 2002). The upper part of the calibration assemblies consisted of an Al_2O_3 thermocouple sleeve inside a MgO cylinder, with the thermocouple at the position of the bottom of the capsule in the melt distribution experiments. The lower part of the graphite furnace consisted of an Al_2O_3 thermocouple sleeve inside a MgO cylinder. After each calibration experiment the whole assembly was sectioned longitudinally in order to measure the spinel layer width every 0.5 mm. Figure 1 shows that the temperatures at the thermocouple and capsule locations are constant within the accuracy of the measurements ($\pm 10°$), so that no correction to the measured temperature is needed.
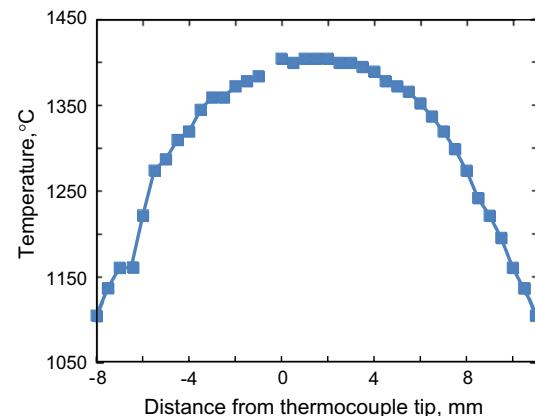

Fig. 1 Temperature distribution along the long axis of the furnace assembly determined from the width of a spinel layer of a calibration experiment at 1400 °C and 1 GPa after 1 week. 0 mm on the *x*-axis indicates the top of the designated capsule location. The *positive* and *negative numbers* represent the distances from the top of capsule toward the *bottom* and *top* of the furnace assembly, respectively. The temperature is within 10 °C from *top* to *bottom* of the designated capsule location (0–4 mm) at the peak of the temperature distribution. The thermocouple is located within this broad maximum; therefore, no correction to the sample temperature is applied

At high temperatures (1350 °C and above), combined with long experimental durations, cracks in the graphite furnace resulting from the initial compression were over time intruded by molten glass. This increased the resistance of the furnace overall and created radial temperature

variations and instability. Experiments that showed a non-homogeneous melt distribution after sectioning were excluded from analysis.

Post-run sample preparation and image processing

Post-run samples were sectioned vertically, vacuum-impregnated in epoxy and polished with diamond paste, then alumina suspension and finally with colloidal silica to produce surfaces free of damage for imaging.

Secondary electron images were obtained on a Zeiss Supra 55 VP SEM at 5–15 kV acceleration voltage and 4.5-mm working distance, with an aperture of 30 μm and relatively high beam currents to promote orientation contrast. Each image consists of 2048 × 1536 pixels with a resolution of 14–29 nm/pixel. This resolution is sufficient for the typical thickness of the melt layers wetting grain boundaries of 100 nm, as discussed below. For each sample, we made mosaics ranging from 8 × 8 to 15 × 10 overlapping images to obtain a representative area, depending on grain sizes (Table 1).

The public domain software ImageJ was used for digital image processing. Melt–solid boundaries were traced on screen for conversion to binary images. Grain boundaries were traced by orientation contrast of neighboring grains and connecting triple junctions to obtain solid–solid boundaries. The mean grain diameter was calculated from the average circle-equivalent grain area in an image and multiplied by $4/\pi$ to correct for sectioning effects of a sphere (Faul and Scott 2006). Dihedral angles for select samples were measured on the same maps. The melt contents shown in Table 1 were also determined from the binary images.

Results

Composition

Selected olivine grains were analyzed by standardized energy-dispersive spectroscopy on the SEM. The compositions range from Mg# 89.9 to 90.1, unchanged from the starting composition of the olivine (see also Faul et al. 2004; Faul and Scott 2006). Glass compositions were not analyzed since they are modified by quench at small melt contents (e.g., Hirose and Kushiro 1993; see "Temperature sensitivity of dihedral angle" section). With the bulk compositions of this study orthopyroxene is present to 1350 °C, decreasing to trace amounts at 1400 °C.

Description of the melt geometry

As further discussed in "Relationship between grain growth and melt geometry" section, the melt geometry needs to
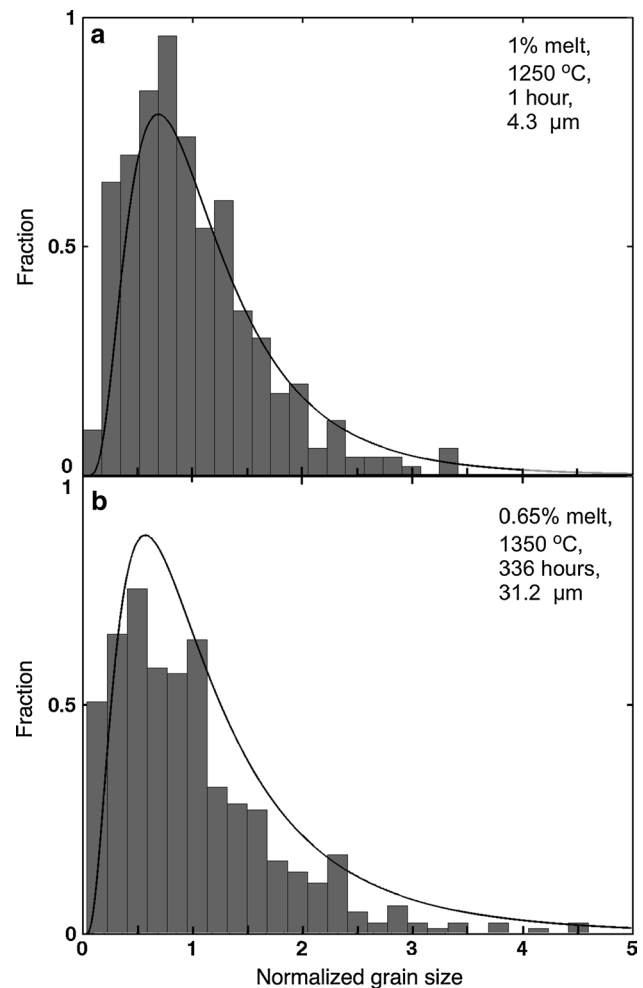

Fig. 2 Histograms of grain size distributions. Grain sizes are normalized by the mean grain size, and the distribution is normalized by its maximum. **a** A fine-grained, short-duration experiment with a mean grain size of 4.3 μm (MELT27). **b** A relatively coarse-grained sample with a mean grain size of 31 μm and 0.6 % melt (MELT22). The *solid line* in both *histograms* shows a lognormal distribution. Comparison of the distribution after 1 h with that after 336 h as well as the lognormal distribution indicates that steady-state grain growth conditions were established at the shortest run duration

be determined for steady-state grain growth conditions. The smallest mean grain size at the end of an experiment in this study is at least four times the starting grain size, so that chemical equilibration and considerable microstructural evolution have taken place from the initial powders. This microstructural evolution is, however, contingent on a small starting grain size (<1 μm, Faul and Jackson 2007, see also Faul 1997). Normalized grain size distributions (Fig. 2) indicate that steady-state grain growth conditions were achieved even at the shortest run durations.

Experimental observations show a change of the melt geometry with increasing melt content at (near) constant grain size (Fig. 3). At 0.6 % (and a grain size of 31 μm)
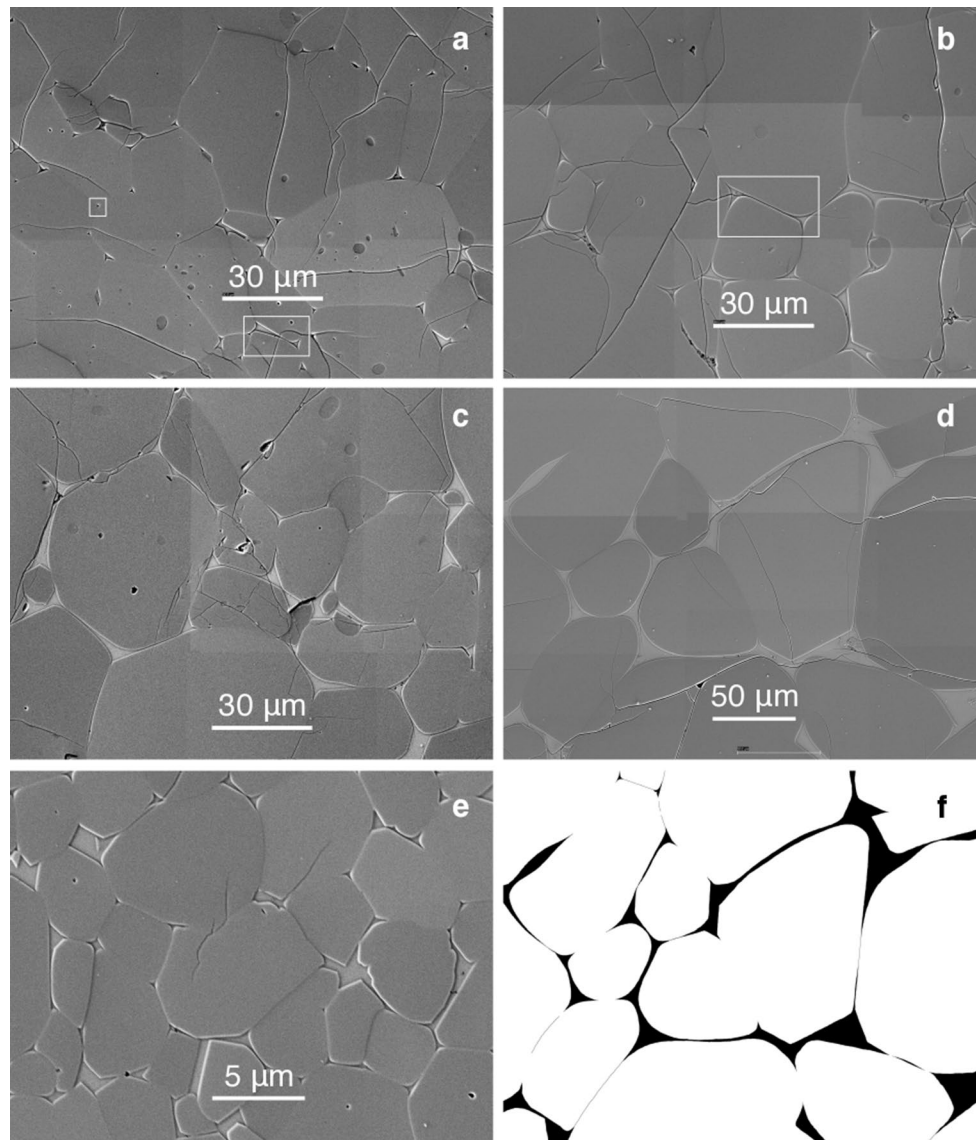
Fig. 3 SEM images representing parts of larger maps from which wetness and grain sizes were measured. The size of the original images can be recognized by *rectangular grayscale* variations. **a–c** The influence of increasing melt content at near-constant grain size (30–40 μm). The predominant melt geometry changes from triple junctions (**a**) to wetted grain boundaries and melt pockets (**c**). **a** 0.6 % melt (MELT22). **b** 1.7 % melt (MELT25). **c** 4.1 % melt (MELT4). **d** The experiment with the coarsest mean grain size and highest melt content in this study (84.5 μm and 6.8 % melt, MELT23) has only few solid–solid grain boundaries remaining, most of the grain boundaries are wetted by melt. **e** Melt distribution in a fine-grained sample (8.6 μm, 3 %, MELT 20). Comparison with **c** at similar melt content but significantly larger grain size illustrates the changes in melt distribution with increasing grain size toward increasing wetness. **f** The binary version of **d**. *Rectangles* in **a** and **b** indicate areas shown enlarged in Fig. 4a, d, respectively

most of the melt resides in triple junctions (Fig. 3a), but their size varies considerably (see "Melt distribution at low melt contents" section). Most triple junctions have a diameter of 1 μm or less (Figs. 3a, 4d), but infrequent, significantly larger, irregular pockets extend over 10 μm (Fig. 4d). No correlation between the size of triple junctions and the size of adjacent grains is observable, although small grains are more frequently associated with larger pockets at this melt content (e.g., Fig. 3a).

At 1.7 % melt penetrates further onto grain boundaries at a similar grain size (Figs. 3b, 4a). Some neighboring triple junctions are connected by melt layers, indicating fully wetted grain boundaries with a dihedral angle of 0°. Larger melt pockets occur at four or more grain corners. At higher melt contents and particularly at coarse grain sizes, the majority of the grain boundaries tend to be wetted by melt (Fig. 3c, d). While crystal–melt interfaces of coarse-grained aggregates are frequently rounded,
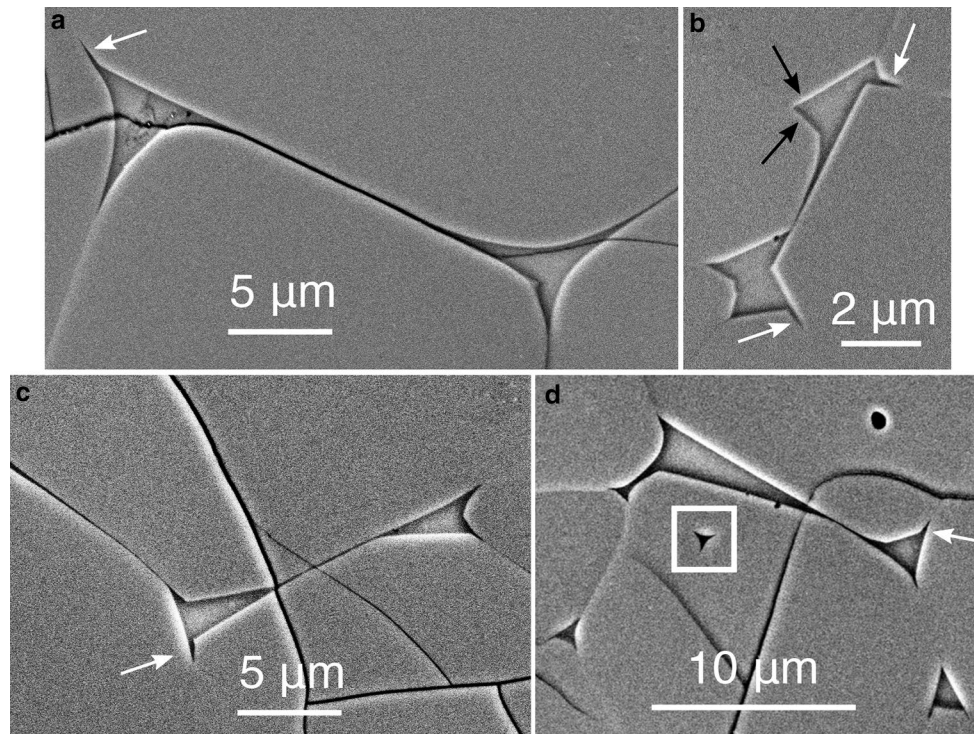
Fig. 4 Higher magnification details of the melt geometry. **a**, **d** Enlarged from the images in Fig. 3b and a, respectively. **a**, **c** Wetted grain boundaries from MELT25 (center of Fig. 3b), and MELT4, respectively. These layers have a thickness of order 100 nm. **b** Faceting at small mean grain size (MELT20). While some faceting is observable at larger grain sizes, it is much more common at grain sizes near or below 10 µm. The junction of two facets forms a large dihedral angle (*black arrows*; see also Cmíral et al. 1998; compare to dihedral angles in **a**, **c**). Parallel-sided, wetted grain boundaries are not observed at fine grain sizes. **d** Larger melt pocket from MELT22 (*rectangle at bottom* of Fig. 3a); the *inset* (*white square*) shows one of the numerous small triple junctions at this melt content at the same scale (*square* at *left* of Fig. 3a), illustrating the size range. Cracks due to quench can easily be distinguished as they cut across grains and melt (glass). The images illustrate that resolution is critical to measuring dihedral angles, as a number of junctions have small extensions into grain boundaries (*white arrows*) yielding angles <10°, which are not resolved at lower magnification (c.f. Cmíral et al. 1998; Faul and Scott 2006)

faceted crystal–melt interfaces dominate at small grain sizes (Figs. 3e, 4b).

In addition to changes with melt fraction, the melt geometry also changes with grain size at approximately constant melt content (Figs. 3c, e, 5). In the fine-grained sample with a mean grain size of 8.6 µm (Fig. 5a) the melt resides predominantly in melt pockets surrounded by faceted crystal–melt interfaces with a range of sizes and shapes. Parallel-sided layers wetting grain boundaries are largely absent. Consistent with these observations, Cmíral et al. (1998) state that the most fine-grained sample in their transmission electron microscope (TEM) study (mean grain size 7 µm) did not contain any wetted grain boundaries. In contrast, at a mean grain size of 40.5 µm (Fig. 5b), wetted grain boundaries are common. The images illustrate that the melt distribution of coarser-grained samples includes more wetted grain boundaries compared to fine-grained samples at the same melt content. The thickness of the layers on grain boundaries does not increase with increasing (mean) grain size, but comparison of Fig. 3c and d suggests that the layer thickness is increased at the comparatively high melt content of 6.8 %.

Figure 4 illustrates that measurement of dihedral angles requires a high enough resolution to image cusps extending into grain boundaries (see also Faul and Scott 2006). Faceting, common at small grain sizes, also results in comparatively large dihedral angles of ~30° (Fig. 4b).

Grain boundary wetness

For a more quantitative assessment of the melt distribution we measured the grain boundary wetness ψ of 18 samples with grain sizes from 4 to 84 µm and melt contents from 0.3 to 6.8 % (Table 1; Fig. 6a). For reference in Fig. 6, grain boundary wetness was also calculated with the idealized isotropic equilibrium model for a rhombic dodecahedral grain shape for dihedral angles from 1° to 30° (von Bargen and Waff 1986; Takei 2002). The grain boundary wetness of experimental samples with a mean grain size smaller than 20 µm falls on the contour predicted by the idealized
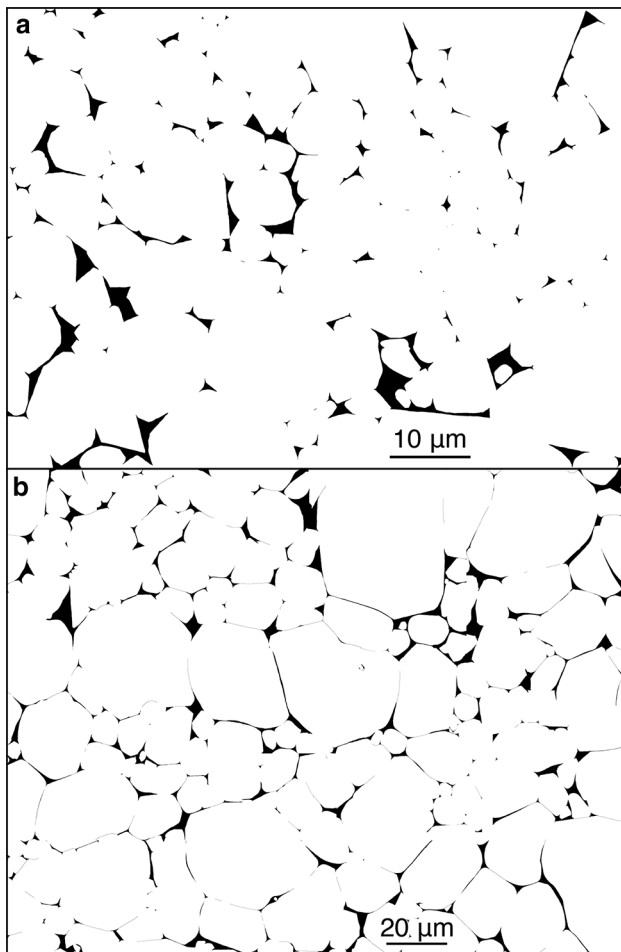
Fig. 5 Influence of mean grain size on the melt distribution. **a** Binary image of a portion of MELT20 with a melt content of 3.8 % and a mean grain size of 8.6 μm. The original image has a resolution of 14 nm/pixel, and the average melt content for this sample is 3 %. **b** Binary image of MELT4 with 4.1 % melt and 40.5 μm mean grain size. The original SEM image has a resolution of 29 nm/pixel. These two images show that coarser-grained samples have more wetted grain boundaries at a similar melt content, and consequently higher grain boundary wetness

model for a dihedral angle of 30° up to a melt content of 2 %. The wetness of samples with grain sizes from 20 to 30 μm falls between the contours for dihedral angles of 1° and 10° to about 2 % melt. Coarse-grained samples (mean grain size >30 μm) with melt contents near 2 % and higher have values for the wetness well above those predicted by the idealized model even for a dihedral angle of 1°. Data from the eutectic system borneol–diphenylamine (Fig. 6b) also show wetness values that exceed those calculated for the idealized system (Takei 2000, see "Organic analogue systems" section).

The relationship between grain boundary wetness and grain size is shown in Fig. 7. When wetness is plotted as a function of grain size for fixed melt content, wetness is seen to increase with increasing grain size. The rapid increase at the coarsest grain size at 2 % melt reflects the increase in Fig. 6a at this melt content. The melt content at which this steep increase in wetness occurs may depend on grain size, with the increase occurring at a lower melt content for coarser grain sizes.

In order to evaluate a possible dependence of dihedral angle and wetness on temperature, experiments were conducted at (near) constant melt content and a range of temperatures (Fig. 8). At a melt content of 2 % two samples with very similar grain size near 13 μm yield the same dihedral angle and grain boundary wetness (Table 1), even though their experimental temperature differed by 200 °C. The most coarse-grained sample in this figure has the smallest dihedral angle and highest grain boundary wetness, despite a temperature that is 100 °C lower than that of a more fine-grained sample, emphasizing that it is grain size that determines the dihedral angle and wetness, rather than temperature.

Discussion

Limitations of the present study

Large grain sizes together with microstructural maturation require relatively long-duration experiments at high temperature (1350–1400 °C). The graphite in the furnaces used in our study was relatively fine-grained, brittle and stronger than the surrounding materials, leading to the development of fractures in the furnaces during pressurization. As discussed above, at high temperatures glass infiltrated the cracks, increasing the furnace resistance over time to levels where temperature could no longer be maintained and the experiment had to be terminated. We therefore limited the experimental durations to 2 weeks at 1400 °C. A practical low-temperature limit is set by clinopyroxene crystallization below 1250 °C with our basalt composition.

The coincidence of the wetness predicted by the idealized model and the measured wetness at small grain sizes (Fig. 6) illustrates the limitation of using wetness as a parameter to characterize the melt distribution. At small grain sizes the melt resides in relatively isometric pockets bounded by faceted crystal–melt interfaces (Fig. 4b). The surface to volume ratio of this melt geometry is similar to that calculated for melt residing in a triple junction network with constant interfacial curvature. Measuring the wetness cannot discern these differences in the melt geometry. Grain size and melt fraction dependence also create a non-uniqueness, so that both parameters need to be given along with the wetness. However, including all surfaces in a given area into a measure of the melt distribution is preferable over essentially point measurements at selected
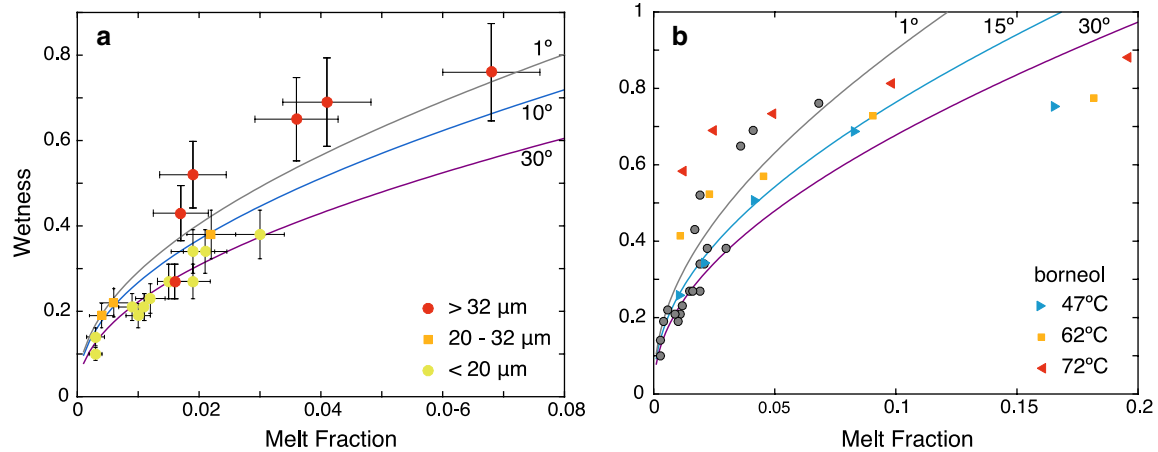
Fig. 6 Grain boundary wetness as a function of melt fraction. The *lines* show grain boundary wetness calculated with the idealized isotropic model for the dihedral angles indicated next to the curves, with equations given by von Bargen and Waff (1986). **a** Data from this study and Garapić et al. (2013). The mean grain size of the samples is distinguished by *colored symbols*. Relatively fine-grained samples (*yellow dots*) fall on the line calculated for a 30° dihedral angle (*purple line*), and medium-grained samples (*orange squares*) follow the *contour line* calculated for a dihedral angle of 10° (*blue line*). Coarse-grained samples (*red dots*) have wetness values well above those predicted by the idealized model at melt fraction above about 0.017. *Error bars* indicate an estimated 15 % uncertainty in the measured values. **b** Comparison of data from this study (*gray dots*) with data from Takei (2000) on the borneol–diphenylamine system extending to higher melt contents. See "Organic analogue systems" section. In this binary system with a bulk composition on the borneol side of the eutectic, the bulk and melt compositions change with temperature such that the borneol content of the melt increases with increasing temperature. The dihedral angle and wetness therefore decrease (Takei 2000)
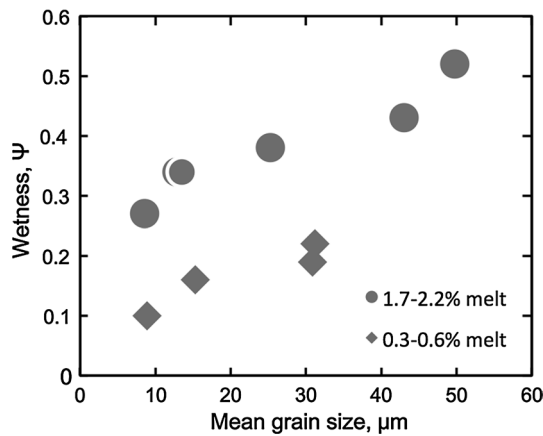

Fig. 7 Grain boundary wetness as a function of mean grain size. *Dots* show experiments with melt contents of around 2 %, diamonds 0.3–0.6 %. The data indicate that grain boundary wetness increases with increasing mean grain size for constant melt content. Comparison with Fig. 6 indicates that the higher wetness of the most coarse-grained sample in this figure reflects the overall increase at this grain size and melt fraction

Fig. 8 Effect of temperature on dihedral angle at a melt content of ~2 %, illustrating that the dihedral angle does not depend on temperature when grain size and melt fraction are fixed. The mean grain size (in μm) of each experiment is indicated above the data points. Two experiments with nearly identical grain size (12.9 and 13.5 μm) have the same grain boundary wetness (Table 1) and dihedral angle (within the error of measurement), although there is a temperature difference of 200 °C. The figure shows that dihedral angle does depend on grain size, as does wetness (Fig. 7)

locations (dihedral angles) for characterization of the melt geometry. Wetted grain boundaries (i.e., dihedral angles of zero degrees) are typically not included in distributions of measured dihedral angles.

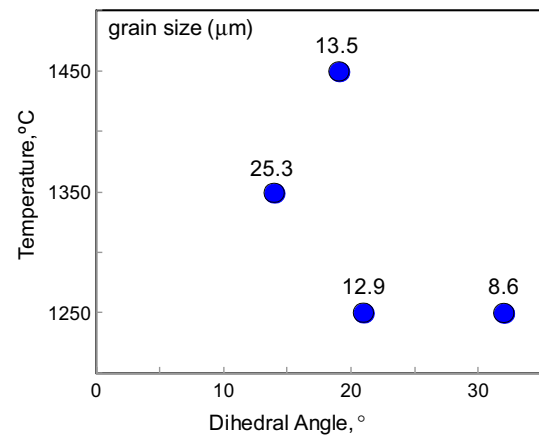Uncertainties in the measured values for wetness, grain size and melt content arise principally from the limited areas that were digitized for each sample. Automated thresholding is not reliable due to grayscale ranges of the melt phase (large pockets are bright due to higher mean atomic number of the melt, and thin layers and small triple junction tend to be darker due to edge effects),

necessitating manual digitization of the interfaces (Garapić et al. 2013). An indication of the uncertainty in the values may be obtained by measuring the parameters from subsets of the final area used for the measurements. This suggests uncertainties up to 15 % of the measured values (indicated in Fig. 6), although the uncertainty should decrease with increasing area.

Comparison with previous studies

The importance of resolution for observation of the melt geometry has been pointed out previously. Cmíral et al. (1998) showed from high-resolution TEM images that true dihedral angles (for which the grain boundary was oriented parallel to the electron beam vs. apparent angles in a 2D section) between olivine and basaltic melt have values of 10° or below. By contrast, earlier studies using light microscopy to measure dihedral angles reported much larger values for the same system (50°, Waff and Bulau 1979). Dihedral angle measurements on SEM images of fine-grained, facetted samples yielded values near 30° (Daines and Kohlstedt 1993). Garapić et al. (2013) demonstrated with high-resolution SEM imaging and serial sectioning that the thin layers on grain boundaries observed earlier (Faul et al. 1994; Faul 1997; Faul and Scott 2006), as well as in this study, are indeed wetted grain boundaries.

Similarly, grain boundary wetness will be underestimated at insufficient resolution, particularly if layers on grain boundaries are not resolved. TEM observations show that the melt layers on grain boundaries are typically around 100 nm thick, layers thinner than 50 nm are rarely observed, and layers or films <10 nm thick are absent (Cmíral et al. 1998; Faul et al. 2004). The resolution of this study is 14–29 nm per pixel, while Yoshino et al. (2005) imaged their samples with resolutions ranging from 60 to 300 nm/pixel, and Zhu et al. (2011) in their synchrotron study had a resolution of 700 nm/voxel (Wark et al. (2003) did not provide any information on their resolution). Thin layers on grain boundaries, contributing disproportionally to wetness but little to area (volume) of melt, could not be resolved in these studies, while larger triple junctions and pockets were imaged. These authors concluded therefore that the idealized model provides a sufficient description of the melt geometry (see also "Melt distribution at low melt contents" section).

A dependence of the melt geometry on melt fraction was noted in previous studies. Hirth and Kohlstedt (1995) observed an increase in wetness with increasing melt content in their samples with mean grain sizes ranging from 10 to 18 μm. They observed a large number of wetted grain boundaries at a melt content >5 % with a decrease of the dihedral angle from 38° to close to 0°. A change of the melt distribution as a function of melt content was also noted by Yoshino et al. (2005), who described an increasing number of wetted grain boundaries at melt contents above 2 %.

Organic analogue systems

Takei (2000) examined the organic system borneol–diphenylamine, which has a eutectic with a composition of 83 wt% diphenylamine at 43 °C. The solid end members of this system exhibit no mutual solubility. The compositions in the experiments were constrained to have borneol as the solid phase. In the eutectic system, obtaining similar melt contents at different temperatures requires a change in the bulk composition. The lowest temperature experiments (47 °C) therefore had a liquid composition furthest from borneol, while with increasing temperature the bulk and liquid compositions move closer to borneol. The samples were annealed at elevated temperatures to reach mean grain sizes of about 100 μm. Wetness was determined semiquantitatively by a "needle-sticking test."

With this analytical difference in mind, the data indicate that the wetness of the lowest temperature sample falls on the contour line for a 15° dihedral angle up to a melt content of about 10 % (Fig. 6b). The measured dihedral angle at this temperature has a value of ~35° (Takei 2000). At higher temperatures melt extends further onto and wets some (but not all) grain boundaries (Takei 2000), similar to the observations for olivine plus basalt. Correspondingly the wetness increases beyond the predictions of the idealized model. The observed temperature dependence of the dihedral angle and wetness of this system is a consequence of the liquid composition moving closer to the composition of (solid) borneol with increasing temperature.

A question remains why the wetness at 47 °C does not increase beyond the idealized model, despite the coarse grain size. Borneol is likely not as anisotropic in its properties as olivine, so that at the relatively large dihedral angle small differences in surface energies for different grain boundary plane orientations are not enough to result in wetting of some grain boundaries (see below). At the higher-temperature compositions the dihedral angle decreases (~17° at 60 °C, Takei 2000), resulting in replacement of some grain boundaries by melt. This increases the overall wetness beyond the isotropic model, as for partially molten dunite. At 72 °C, with a dihedral angle near 0° (Takei 2000), solid grain boundaries are quickly replaced by melt with increasing melt content, resulting in a steeply increasing wetness at low melt contents.

Comparison of the wetness of the silicate and the organic system (Fig. 6b) suggests that the organic system is more similar to partially molten dunite at higher temperatures (62 and 72 °C) than at 47 °C. However, McCarthy and Takei (2011) measured seismic properties of the

borneol–diphenylamine system at 47 °C. They did not observe a peak in attenuation, in contrast to Jackson et al. (2004) for partially molten dunite. The microstructural observations at 47° suggest that wetted grain boundaries are essentially absent, which means that melt squirt takes place at frequencies higher than those used in the experiments (Faul et al. 2004). In contrast, wetted grain boundaries with much lower aspect ratios, as observed for partially molten dunite (Garapić et al. 2013), result in melt squirt in the experimental frequency range. The differences in microstructure may therefore explain the different experimental observations of McCarthy and Takei (2011) and Jackson et al. (2004).

Wetness levels off at values between 0.8 and 0.9 at melt contents above 5 %, while the idealized model predicts complete wetting for dihedral angles <20° at this melt content (Fig. 6b). The observations indicate that not all grain boundaries will be wetted by melt even at high melt contents, suggesting that the remaining melt-free grain boundaries have low grain boundary energies. This can explain the formation of clusters of crystalline grains even at high liquid fractions, for example in extrusive rocks. In addition, the melt content for disaggregation, where all intergranular contact is lost, is higher than predicted by the idealized model for dihedral angles <30°.

Temperature sensitivity of dihedral angle and grain boundary wetness

Yoshino et al. (2009) reanalyzed the 1-GPa experiments with a lherzolite composition of Yoshino et al. (2005) and conducted additional experiments at higher pressures to examine the melt distribution. They observed a decrease of the dihedral angle with increasing temperature to values near zero at the highest temperatures in their study (1500–1720 °C). In contrast to the starting composition of the present experiments with olivine and a fixed amount of basaltic melt, Yoshino et al. (2009) examined the melt distribution as a function of temperature for a fixed lherzolite starting composition. For a lherzolite at fixed pressure the melt content will increase with increasing temperature as the pyroxene mode decreases (e.g., Baker and Stolper 1994; Walter 1998). As shown in Yoshino et al. (2005, Table 1, KLB1 composition) with increasing temperature the melt content increases from 2.4 % at 1200 °C to 30 % at 1350 °C with a concomitant increase in grain size from 13 to above 50 μm.

Yoshino et al. (2009) ascribe the observed decrease of the dihedral angle to a change of the melt composition (decrease of polymerization of the melt) with temperature in their experiments. They analyzed their melt compositions directly on their charges with a defocused beam. However, problems with quench modification of interstitial

melt have long been recognized in the petrological literature (e.g., Jaques and Green 1979; Hirose and Kushiro 1993; Baker and Stolper 1994). The Mg# given by Yoshino et al. (2009) increases from 45 at 1200 °C (2.4 % melt) to 73 at 1400 °C. By comparison, Baker and Stolper (1994) reported glass compositions from diamond traps as Mg# of 75.6 at 1270 °C increasing to 79.2 at 1390 °C. Similarly, Laporte et al. (2004) report glass Mg# from 72.3 to 77.4 at temperatures from 1220 to 1360 °C. This comparison indicates that the large increase of the Mg# observed by Yoshino et al. (2009) is due to quench modification of the melt (see, e.g., their Fig. 1d; note that for the purposes of digitizing the melt–solid interface, quench crystallization can easily be identified in the images, as discussed by Yoshino et al. (2009)). The increase in the Mg# reported by Yoshino et al. (2009) between 1200 and 1400 °C mirrors the decrease in polymerization shown in their Fig. 4. The significantly smaller change in Mg# observed by Baker and Stolper (1994) and Laporte et al. (2004) implies that any compositional effects on the dihedral angle will be correspondingly smaller.

We measured dihedral angles over a temperature range from 1250 to 1450 °C on experiments with similar melt contents (about 2 %). As Fig. 8 shows, no temperature dependence is evident over this temperature interval. The dihedral angle for the most coarse-grained sample measured in this study is consistent with those by Faul and Scott (2006), and at high resolution by Cmíral et al. (1998) over a temperature range from 1200 to 1450 °C for coarse-grained samples. Samples with a mean grain size below 10 μm have larger dihedral angles, due to the larger number of junctions formed by facetted crystal–melt interfaces (c.f. Fig. 4b). Figure 8 also shows that the dihedral angle is grain size dependent, as is wetness (Fig. 7). We therefore conclude that the observed change in dihedral angle in Yoshino et al. (2009) is due to the compounding effects of melt content and grain size increasing with increasing temperature in their study. No temperature dependence of wetness or dihedral angle can be resolved at temperatures up to 1450 °C when grain size and melt fraction are accounted for in partially molten dunite. This contrasts with the organic system borneol + diphenylamine where the liquid composition changes with temperature (Takei 2000).

Relationship between grain growth and melt geometry

The assumptions made with the idealized model of the melt distribution are a static, uniform grain size with a space-filling geometry and crystalline isotropy. Consequences of these assumptions are that the melt distribution is self-similar, static and independent of melt fraction and grain size. Surface energy minimization only affects the local geometry at the junction of two grains and melt, i.e., the dihedral angle.

However, in polycrystalline aggregates surface energy minimization drives an increase in mean grain size with time, i.e., grain growth (Atkinson 1988; German et al. 2009). For a given volume, the increase in mean grain size implies that the total number of grains in this volume is decreasing, i.e., some grains shrink and disappear, while others grow. The disappearance of grains means that grains that were not in contact before now have to form a common grain boundary. Since silicate crystals are not isotropic in their properties, the energetically most favorable grain boundary plane orientation depends on the orientation of both neighboring crystalline grains. Further complications are that a single surface of a large grain may be in contact with more than one smaller grain, and that a growing grain may be next to a shrinking grain. In this system therefore grain boundary plane orientations are constantly changing and may not immediately be the lowest energy orientation for two neighbors. German et al. (2009) note that for a dihedral angle of 30° a decrease of the solid–liquid surface energy of only 7 % is needed for the liquid to wet a grain boundary. Grain boundary planes that are not in their minimum energy orientation may therefore be wetted by melt, as is observed experimentally.

Grain growth in a melt-bearing system can be observed directly in experiments with an analogue system of norcamphor and ethanol (Walte et al. 2003). The experiments show that in response to grain growth the melt in the system moves around, transiently producing wetted grain boundaries (e.g., their Fig. 3), even in a near-isotropic system with a dihedral angle that is larger than that of the olivine–basalt system. Walte et al. (2003) emphasize the transient nature of the wetted grain boundaries, but also that due to their slow disappearance and the continuous nature of grain growth they will always be part of the system. For olivine the establishment of slow growing, faceted crystal–melt interfaces stabilizes larger melt pockets, increasing the grain scale heterogeneity of the melt distribution (Waff and Faul 1992). Grain growth proceeding with a stationary normalized grain size distribution is referred to as steady-state growth, with corresponding steady-state (but not static) melt distribution, which includes wetted grain boundaries.

Samples with small (mean) grain sizes show extensive faceting of crystal–melt interfaces (Figs. 3e, 4b, also, e.g., Figure 3 of Hirth and Kohlstedt 1995; Figure 5 of Mei et al. 2002). The extensive faceting is due to the faster absolute growth rates as well as adjustment of grain boundary plane orientations, which allows expression of the preferred crystal habit. Similarly, isolated grains or small clusters of phenocrysts surrounded by melt or a fine groundmass in extrusive rocks can develop their ideal crystal habit. Dihedral angles measured in faceted systems, both experimental (e.g., Daines and Kohlstedt 1993) and natural ones (Holness 2006), yield values of 30°, but are not representative of coarse-grained mantle rocks at low melt contents.

Wetted grain boundaries are observed as a result of liquid phase sintering, for which samples are not encapsulated but open to the surrounding atmosphere (e.g., German et al. 2009). Moreover, initially melt-free oxides infiltrated by a melt from the outside show wetted grain boundaries (Beere 1974). Wetted grain boundaries are therefore not an artifact of encapsulation (over-pressurized closed system).

Melt distribution at low melt contents

As described in "Grain boundary wetness" section, triple junction tubules are common at a melt content of 0.6 % at a relatively coarse grain size of 31.2 µm (MELT22). The wetness for this sample falls between the values calculated for the idealized model with dihedral angles between 1° and 10° (Fig. 6a). To characterize the melt distribution further, we determined the proportion of melt by area of the total melt area for different size ranges of individual melt pockets (triple junctions and larger pockets). This analysis is possible at low melt contents where wetted grain boundaries connecting adjacent triple junctions are relatively rare.

We divided the melt pockets of this sample into six size ranges by their equivalent circle diameter, which was calculated from the measured area of the individual pockets. This allows determination of the fraction of the total number of melt pockets in a certain size range, as well as the area fraction of melt contained in these pockets (Fig. 9). The largest pockets, those with an equivalent circle diameter greater than 4.9 µm, constitute 2.4 % of the total number of inclusions but contain just over 30 % of the total melt area. These large pockets are typically surrounded by more than three grains (Fig. 4d) and are associated with small grains (Fig. 3a), consistent with the notion that these grains are shrinking (Walte et al. 2003). Pockets in the size range from 3 to 4.9 µm (predominantly large triple junctions) constitute 6.7 % of the total number of pockets and contain an additional 30 % of the melt by area. Pockets with a diameter <0.7 µm (essentially triple junctions only) constitute nearly 40 % of the total number of inclusions, but contain only about 3.3 % of the area of melt.

If a diameter of at least two voxels is needed to resolve triple junction tubules by X-ray microtomography (i.e., tubules with an equivalent diameter of 1.4 µm at a resolution of 0.7 µm, Zhu et al. 2011) 70 % of all triple junction tubules could not be resolved in this sample. The observation of 50 % singly connected four-grain corners at a melt content of 2 % (Zhu et al. 2011) implies that the majority of triple junctions joining these corners are too small to be resolved, consistent with the analysis presented here. The transport properties at low melt contents can therefore not be determined from X-ray microtomography images.

Figure 9 shows that the largest 9 % of all pockets contain 60 % of the melt, while the smallest 70 % contain only
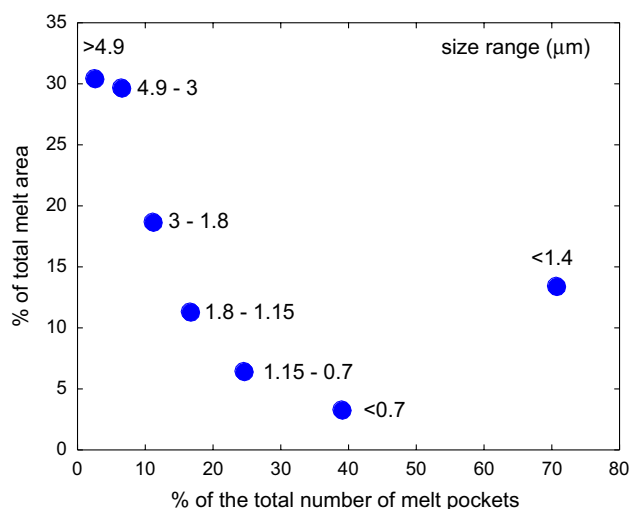
Fig. 9 Fraction of the total number of melt pockets sorted by size of sample MELT22. The *y*-axis shows the fraction of the total melt area contained in each size range. The sizes represent equivalent circle diameters calculated from the areas of individual pockets. Pockets >4.9 μm are surrounded by more than three grains (Fig. 4b), while the smaller sizes are mostly triple junction tubules. Additionally the data point <1.4 μm was calculated to show that these triple junctions constitute 70 % of all melt pockets but contain only 13 % of the melt area

13 % of the melt. Nearly three quarters of all three-grain edge tubules, constituting the connected network of melt, therefore contain an equivalent melt content of only 0.08 % in this sample with an overall melt content of 0.6 %. Consequently it is the size of these small triple junctions that determines the transport properties of the system. Calculating permeability with a triple junction diameter based on the total melt content of 0.6 % therefore overestimates it, as inferred by Faul (2001).

Volatile-rich melts

There are only few microstructural studies on volatile-rich and particularly carbonate melts. A single experiment was reported by Hunter and McKenzie (1989), conducted in a temperature gradient on a harzburgite with carbonate melt present. The starting material was ground to very fine grain size (<2 μm). The microstructure shown for an area with a grain size <10 μm and melt content of 6–8 % is similar to that in Fig. 3e with a comparable grain size. Corresponding to the relatively small grain size and high melt fraction, faceting is pronounced, and the melt predominantly resides in larger pockets separating neighboring grains. The reported dihedral angle of 28° is similar to the dihedral angle of the most fine-grained sample of this study (Fig. 8).

Minarik and Watson (1995) showed that carbonate melt is connected to at least 0.05 %, but their experiments

were aimed at determining diffusivity, with corresponding chemical and microstructural disequilibrium. Faul (1997) showed in experiments with similarly coarse starting grain size that the grain size distribution even after >300 h at 1300 °C did not reach a steady-state distribution.

The observations from olivine plus carbonate melt therefore indicate that the overall melt distribution is similar to the system olivine–basaltic melt, including connectivity to vanishingly small melt content. Faul et al. (2004) showed with TEM observations that even at a (basaltic) melt content of 0.01 % nearly all triple junctions contained melt, demonstrating that the melt is connected at this melt content. The observations regarding the melt distribution presented here therefore likely apply to carbonate melt as well. Due to the much lower viscosity and density, carbonate melts are expected to be significantly more mobile (e.g., Faul 2001).

The similarity of the melt geometry of carbonate melt is due to the substantial solubility of silicates, as evidenced by the reported melt compositions. This is consistent with the observations of Yoshino et al. (2007) who conducted experiments with olivine + hydrous fluid, and showed that the dihedral angle decreases as a function of pressure due to the increasing solubility of silicates in the fluid (e.g., Bureau and Keppler 1999).

Implication for the viscosity of the upper mantle

Diffusion creep experiments are carried out with fine-grained aggregates (typically <15 μm) in order to avoid the transition to dislocation creep at experimentally accessible stresses and strain rates. Melt distribution and faceting in these experiments are comparable to the fine-grained samples of this study (Figs. 3e, 4b; compare to Figure 3 of Hirth and Kohlstedt 1995; Figure 5 of Mei et al. 2002). However, the melt geometry changes as a function of grain size (Figs. 3, 5, 7). While coarser-grained samples cannot be deformed in diffusion creep at laboratory conditions, the melt distribution observed with coarse grain sizes in this study, more specifically the wetness, can be used to calculate the viscosity with the model of Takei and Holtzman (2009a, b abbreviated as TH9a, b).

Takei (1998) examined the relationship between macroscopic mechanical properties and microscopic geometry of solid–liquid composites. She concluded that grain boundary contiguity φ ($\varphi = 1 - \psi$, i.e., 1 − wetness) is the primary factor that determines the macroscopic properties of granular composites. The melt content affects the properties of the aggregate only indirectly through grain boundary contiguity. TH9a developed this model further to derive constitutive relations for partially molten rocks deforming by grain boundary diffusion creep (termed contiguity model). When finite liquid diffusivity and reaction
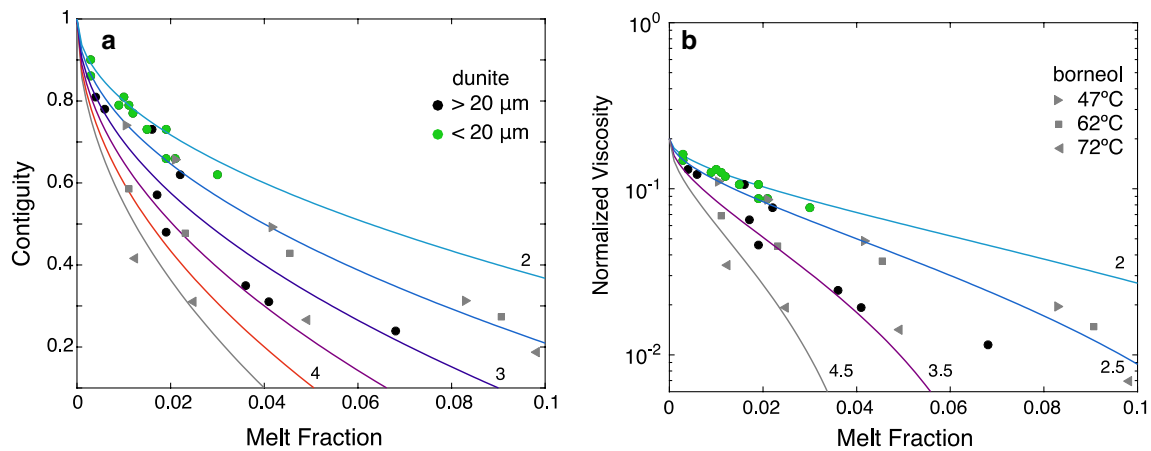
Fig. 10 Contiguity (**a**) and normalized viscosity (**b**) plotted as a function of melt fraction. *Dots* represent data from this study, *triangles* and *squares* borneol–diphenylamine (Takei 2000), lines are calculated with equations given in Takei and Holtzman (2009a) (see text). Values for the parameter *A* in Eq. (2) for contiguity are shown in the figure next to the lines. $A = 2$ corresponds to a dihedral angle of approximately 30° in the idealized model, $A = 2.5$ corresponds to 15°, and $A > 3$ indicates contiguity smaller than that for a dihedral angle of 1° in the idealized model. Comparison of the normalized viscosities shows that coarse-grained samples are significantly weaker at the same melt fraction compared to fine-grained samples. The even coarser-grained borneol samples (see Fig. 6b) indicate a rapid drop in viscosity at melt contents up to about 2 % for the highest temperature composition. At higher melt contents the viscosity decreases much more modestly with melt content

rates are included at low melt contents, this model predicts a decrease in viscosity from melt-free conditions to a melt content of 1 % by one order of magnitude (TH9a, b).

Diffusion occurs through and is limited by grain boundary diffusivity in melt-free aggregates. This is indicated by an experimentally observed cubic dependence of strain rate on grain size (e.g., Hirth and Kohlstedt 1995; Faul and Jackson 2007). Grain boundaries in olivine are about 1 nm wide (Vaughan et al. 1982; Faul et al. 2004) and are enriched in trace elements relative to olivine interiors (Drury and Fitz Gerald 1996; Hiraga et al. 2002; Faul et al. 2004), providing fast diffusion pathways relative to grain interiors. In the contiguity model, at the onset of melting, melt is located in tubules with a cross-sectional area that is not significantly larger than the cross-sectional area of (melt free) grain boundaries (TH9a; Holtzman 2016). With increasing melt content the tubule size increases, leading to a transition where diffusion in the melt network becomes faster than through grain boundaries (and small tubules). At this stage bulk diffusion becomes limited by transport through grain boundaries to the nearest tubule. This rapid increase in effective bulk diffusivity causes an equally rapid drop in viscosity at small melt contents. The melt content necessary for the transition to occur decreases with increasing grain size, since the tubule size depends linearly on grain size (e.g., Holtzman 2016). The prediction of a large decrease in strength of rocks at the onset of melting is consistent with prior experimental observations that show a substantial increase in strain rates in the diffusion creep regime for the first percent of melt (Faul and Jackson 2007).

The TH9a, b model is substantially based on the geometry of the idealized model to calculate the efficiency of diffusion pathways. Following von Bargen and Waff (1986), TH9a calculates contiguity as a function of melt fraction for different space-filling grain geometries and dihedral angles. They then use a semiempirical equation to simplify this relationship:

$$\varphi = 1 - A\,\phi^{1/2}, \tag{2}$$

ϕ is the melt fraction, and A is a constant. The value of A changes with dihedral angle from $A = 2$ for a dihedral angle $\theta = 30°$ to $A = 2.3$ for $\theta = 20°$ (TH9a, their Figure 11). As Fig. 6 shows, the experimentally measured wetness exceeds that predicted for the idealized model even for a dihedral angle of 1°. To match the experimentally observed contiguity, the parameter A in Eq. 2 is varied from 2 to 4.5 (Fig. 10a). The more coarse-grained olivine–basalt samples fall on the curve for $A = 3.5$. The borneol samples at 62° and 72 °C with a grain size of 100 μm suggest that at coarser grain size contiguity increases more rapidly at melt contents below 2 %.

The (normalized) viscosity is calculated from contiguity with Equation 45 of TH9a for contiguity calculated from Eq. 2, as well as from the experimentally measured contiguities and melt fractions (Fig. 10b). While the data are scattered, Fig. 10b indicates that for grain sizes <20 μm the decrease in viscosity due to increasing melt fraction is adequately approximated by $A = 2$, which from Fig. 10a corresponds to a dihedral angle of 30° of the idealized model. For grain sizes >20 μm the olivine + basalt data and the

$62°$ borneol data fall on the curve calculated with $A = 3.5$. This value of A is larger than that in the idealized model for a dihedral angle of $1°$ (Fig. 6) and shows a rapid decrease in creep strength with melt fraction. The viscosity decrease then levels off at higher melt contents, corresponding to the leveling off of wetness (Fig. 6b).

In diffusion creep the presence of melt therefore reduces the strength of partially molten rocks more quickly than experiments with fine grain sizes indicate. At a melt content of 2 % and a grain size of 30 µm the calculated viscosity approaches a value of 1/3 of the more fine-grained samples typically used in experiments. Figure 10b suggests that at even lower melt contents the viscosity decreases more rapidly for larger grain sizes than the experimental observations from fine-grained aggregates indicate. The grain sizes of this study, while significantly larger than those used in diffusion creep experiments, are still a factor of 10–100 smaller than grain sizes inferred for the upper mantle. If wetness continues to increase at fixed melt content with increasing grain size as suggested by Fig. 7 (and the borneol data), the viscosity at mantle grain sizes will decrease even more rapidly at small melt contents. Diffusion creep may therefore play an important role in partially molten regions of the upper mantle.

A remaining question is whether deformation will lead to a stress-controlled melt distribution (Daines and Kohlstedt 1997; Holtzman et al. 2003). The analysis of TH9a, b suggests that diffusion quickly becomes efficient even at melt contents below 0.01 % at mantle grain sizes. Deformation experiments by necessity are conducted at strain rates more than seven orders of magnitude higher than strain rates expected for the upper mantle. Diffusive processes such as grain growth may therefore be fast enough to alleviate a convective stress-driven melt distribution, which will remain controlled by surface energy.

Conclusions

This experimental study of the melt geometry and distribution in partially molten dunite shows that characterization by dihedral angle alone is not adequate for the determination of bulk rock properties. The assumption of the idealized isotropic model of a static system with a single grain size is not representative of natural systems with grain size distributions resulting from continuing grain growth. We characterized the melt distribution at low melt contents by measuring grain boundary wetness, a parameter, while not unique, that captures changes in the grain scale melt distribution with melt content and grain size.

The experimentally measured wetness increases with increasing melt content to values well above those predicted by the idealized model. Additionally, at constant melt content, grain boundary wetness increases with increasing grain size, in contrast to the assumption of a self-similar melt distribution in the idealized model. No temperature sensitivity of the dihedral angle or the melt geometry is observed when grain size and melt fraction as factors influencing the melt distribution are accounted for. The experimental observations suggest that wetness increases more quickly as a function of melt content at mm to cm grain sizes inferred for the upper mantle. With the experimentally measured wetness the shear viscosity calculated with the solid–liquid composite model of Takei and Holtzman (2009a) decreases more quickly than predicted by the idealized model at melt contents of the order of percent. This enhances diffusion creep at small melt fractions relative to dislocation creep in partially molten regions of the upper mantle.

References

Atkinson HV (1988) Theories of normal grain growth in pure single phase systems. Acta Metall 36:469–491

Baker MB, Stolper EM (1994) Determining the compositions of high-pressure melts using diamond aggregates. Geochim Cosmochim Acta 58:2811–2827

Beere W (1974) A unifying theory on the stability of penetrating liquid phases and sintering pores. Acta Metall 23:131–138

Bulau JR, Waff HS, Tyburczy JA (1979) Mechanical and thermodynamic constraints on fluid distribution in partial melts. J Geophys Res 84:6102–6108

Bureau H, Keppler H (1999) Complete miscibility between silicate melts and hydrous fluids in the upper mantle: experimental evidence and geochemical implications. Earth Planet Sci Lett 165:187–196

Cmíral M, Fitz Gerald JD, Faul UH, Green DH (1998) A close look at dihedral angles and melt geometry in olivine-basalt aggregates: a TEM study. Contrib Mineral Petrol 130:336–345

Cooper RF, Kohlstedt DL (1982) Interfacial energies in the olivine–basalt system. Adv Earth Planet Sci 12:217–228

Daines MJ, Kohlstedt DL (1993) A laboratory study of melt migration. Philos Trans R Soc Lond 342:43–52

Daines MJ, Kohlstedt DL (1997) Influence of deformation on melt topology in peridotites. J Geophys Res 102:10257–10271

Drury MR, Fitz Gerald JD (1996) Grain boundary melt films in an experimentally deformed olivine–orthopyroxene rock: implications for melt distribution in upper mantle rocks. Geophys Res Lett 23:701–704

Faul UH (1997) Permeability of partially molten upper mantle rocks from experiments and percolation theory. J Geophys Res 102:10299–10311

Faul UH (2001) Melt retention and segregation beneath mid-ocean ridges. Nature 410:920–923

Faul UH, Jackson I (2007) Diffusion creep of dry, melt-free olivine. J Geophys Res. doi:10.1029/2006JB004586

Faul UH, Scott D (2006) Grain growth in partially molten olivine. Contrib Mineral Petrol 151:101–111. doi:10.1007/s00410-005-0048-1

Faul UH, Toomey DR, Waff HS (1994) Intergranular basaltic melt is distributed in thin, elongated inclusions. Geophys Res Lett 21:29–32

Faul UH, Fitz Gerald JD, Jackson I (2004) Shear wave attenuation and dispersion in melt-bearing olivine polycrystals: 2. Microstructural interpretation and seismological implications. J Geophys Res. doi:10.1029/2003JB002407

Freda C, Baker DR, Ottolini L (2001) Reduction of water loss from gold-palladium capsules during piston-cylinder experiments by use of pyrophyllite powder. Am Mineral 86:234–237

Garapić G, Faul UH, Brisson E (2013) High resolution imaging of the melt distribution in partially molten upper mantle rocks: evidence for wetted two-grain boundaries. Geochem Geophys Geosys. doi:10.1029/2012GC004547

German RM, Suri P, Park SJ (2009) Review: liquid phase sintering. J Mater Sci 44:1–39

Hiraga T, Anderson IM, Zimmerman ME, Mei S, Kohlstedt DL (2002) Structure and chemistry of grain boundaries in deformed, olivine + basalt and partially molten lherzolite aggregates: evidence of melt-free grain boundaries. Contrib Mineral Petrol 144:163–175

Hirose K, Kushiro I (1993) Partial melting of dry peridotites at high pressure: determination of composition of melts segregated from peridotite using aggregates of diamond. Earth Planet Sci Lett 114:447–489

Hirth G, Kohlstedt DL (1995) Experimental constraints on the dynamics of the partially molten upper mantle: deformation in the diffusion creep regime. J Geophys Res 100:1981–2001

Holness MB (2006) Melt–solid dihedral angles of common minerals in natural rocks. J Petrol 47:791–800

Holtzman BK (2016) Questions on the existence, persistence, and mechanical effects of a very small melt fraction in the asthenosphere. Geochem Geophys Geosys. doi:10.1002/2015GC006102

Holtzman BK, Kohlstedt DL, Zimmerman ME, Heidelbach F, Hiraga T, Hustoft J (2003) Melt segregation and strain partitioning: implications for seismic anisotropy and mantle flow. Science 301:1227–1230

Hunter RH, McKenzie D (1989) The equilibrium geometry of carbonate melts in rocks of mantle composition. Earth Planet Sci Let 92:347–356

Jackson I, Fitz Gerald JD, Faul UH, Tan BH (2002) Grain-size—sensitive seismic wave attenuation in polycrystalline olivine. J Geophys Res. doi:10.1029/2001JB001225

Jackson I, Faul UH, Fitz Gerald JD, Tan BH (2004) Shear wave attenuation and dispersion in melt-bearing olivine polycrystals: 1 Specimen fabrication and mechanical testing. J Geophys Res. doi:10.1029/2003JB002406

Jaques AL, Green DH (1979) Determination of liquid compositions in high-pressure melting of peridotites. Am Mineral 64:1312–1321

Karato S (1989) Grain growth kinetics in olivine aggregates. Tectonophysics 168:255–273

Laporte D, Toplis MJ, Seyler M, Devidal JL (2004) A new experimental technique for extracting liquids from peridotite at very low degrees of melting: application to partial melting of depleted peridotite. Contrib Mineral Petrol 146:463–484

Lesher CE, Walker D (1988) Cumulate maturation and melt migration in a temperature gradient. J Geophys Res 93:10295–10311

McCarthy C, Takei Y (2011) Anelasticity and viscosity of partially molten rock analogue: toward seismic detection of small quantities of melt. Geophys Res Lett. doi:10.1029/2011GL048776

Médard E, McCammon CA, Barr JA, Grove TL (2008) Oxygen fugacity, temperature reproducibility, and H_2O contents of nominally anhydrous piston-cylinder experiments using graphite capsules. Am Mineral 93:1838–1844

Mei S, Bai W, Hiraga T, Kohlstedt DL (2002) Influence of melt on the creep behavior of olivine–basalt aggregates under hydrous conditions. Earth Planet Sci Lett 201:491–507

Minarik WG, Watson EB (1995) Interconnectivity of carbonate melt at low melt fraction. Earth Planet Sci Lett 133:423–437

Shankland TJ, Waff HS (1977) Partial melting and electrical conductivity anomalies in the upper mantle. J Geophys Res 82:5409–5417

Takei Y (1998) Constitutive mechanical relations of solid–liquid composites in terms of grain boundary contiguity. J Geophys Res 103:18183–18203

Takei Y (2000) Acoustic properties of partially molten media studied on a simple binary system with a controllable dihedral angle. J Geophys Res 105:16665–16682

Takei Y (2002) Effect of pore geometry on V_p/V_s: from equilibrium geometry to crack. J Geophys Res. doi:10.1029/2001JB000522

Takei Y, Holtzman BK (2009a) Viscous constitutive relations of solid–liquid composites in terms of grain boundary contiguity: 1. Grain boundary diffusion control model. J Geophys Res. doi:10.1029/2008JB005850

Takei Y, Holtzman BK (2009b) Viscous constitutive relations of solid–liquid composites in terms of grain boundary contiguity: 2. Compositional model for small melt fractions. J Geophys Res. doi:10.1029/2008JB005851

ten Grotenhuis SM, Drury MR, Spiers CJ, Peach CJ (2005) Melt distribution in olivine rocks based on electrical conductivity measurements. J Geophys Res. doi:10.1029/2004JB003462

Truckenbrodt J, Johannes W (1999) H_2O loss during piston cylinder experiments. Am Mineral 84:1333–1335

Vaughan PJ, Kohlstedt DL, Waff HS (1982) Distribution of the glass phase in hot-pressed, olivine–basalt aggregates; an electron microscopy study. Contrib Mineral Petrol 81:253–261

von Bargen N, Waff HS (1986) Permeabilities, interfacial areas and curvatures of partially molten systems: results of numerical computations of equilibrium microstructures. J Geophys Res 91:9261–9276

Waff HS, Bulau JR (1979) Equilibrium fluid distribution in an ultramafic partial melt under hydrostatic stress conditions. J Geophys Res 84:6109–6114

Waff HS, Faul UH (1992) Effects of crystalline anisotropy on fluid distribution in ultramafic partial melts. J Geophys Res 97:9003–9014

Walte ND, Bons PD, Pashier CW, Koehn D (2003) Disequilibrium melt distribution during static recrystallization. Geology 31:1009–1012

Walter MJ (1998) Melting of garnet peridotite and the origin of komatiite and depleted lithosphere. J Petrol 39:29–60

Wark DA, Williams CA, Watson EB, Price JD (2003) Reassessment of pore shapes in microstructurally equilibrated rocks, with implications for permeability of the upper mantle. J Geophys Res. doi:10.1029/2001JB001575

Watson EB, Wark DA, Price JD (2002) Mapping the thermal structure of solid-media pressure assemblies. Contrib Mineral Petrol 142:640–652

Yoshino T, Takei Y, Wark D, Watson E (2005) Grain boundary wetness of texturally equilibrated rocks, with implications for seismic properties of the upper mantle. J Geophys Res. doi:10.1029/2004JB003544

Yoshino T, Nishihara Y, Karato SI (2007) Complete wetting of olivine grain boundaries by a hydrous melt near the mantle transition zone. Earth Planet Sci Lett 256:466–472

Yoshino T, Yamazaki D, Mibe K (2009) Well-wetted olivine grain boundaries in partially molten peridotite in the asthenosphere. Earth Planet Sci Lett 283:167–173

Zhu W, Gaetani GA, Fusseis F, Montési LGJ, Carlo FD (2011) Micro-tomography of partially molten rocks: three-dimensional melt distribution in mantle peridotite. Science. doi:10.1126/science.1202,221